Synchrotron X-ray Imaging of Directed Energy Deposition Additive Manufacturing of Titanium Alloy Ti-6242

Yunhui Chen[1,2], Samuel J. Clark[1,2*], Lorna Sinclair[1,2], Chu Lun Alex Leung[1,2], Sebastian Marussi[1,2], Thomas Connolley[3], Robert C. Atwood[3], Gavin J. Baxter[4], Martyn A. Jones[4], Iain Todd[5], Peter D. Lee[1,2]

[1] Mechanical Engineering, University College London, Torrington Place, London WC1E 7JE, UK

[2] Research Complex at Harwell, Rutherford Appleton Laboratory, Oxfordshire OX11 0FA, UK

[3] Diamond Light Source, Harwell Campus, Oxfordshire, OX11 0DE, UK

[4] Rolls-Royce plc, PO Box 31, Derby, DE24 8BJ

[5] Department of Materials Science and Engineering, Sir Robert Hadfield Building, Mappin Street, Sheffield, S1 3JD

* Current address: Current address: X-ray Science Division, Argonne National Laboratory, 9700 S Cass Ave, Lemont Il USA

Abstract

Directed Energy Deposition Additive Manufacturing (DED-AM) is transformative for the production of larger, geometrically complex metallic components. However, the mechanical properties of titanium alloy DED-AM components do not always reach their full potential due to microstructural features including porosity and regions of lack of fusion. Using *in situ* and *operando* synchrotron X-ray imaging we gain insights into key laser-matter interaction and microstructural feature formation mechanisms during DED-AM of Ti-6242. Analysis of the process conditions reveals that laser power is dominant for build efficiency while higher traverse speed can effectively reduce lack of fusion regions. We also elucidate the

mechanisms underlying several physical phenomena occurring during the deposition of titanium alloys, including the formation of a saddle-shaped melt pool and pore pushing. The findings of this work clarify the transient kinetics behind the DED-AM of titanium alloys and can be used as a guide for optimising industrial additive manufacturing processes.

Keywords: Directed Energy Deposition; Synchrotron X-ray imaging; Laser Additive Manufacturing, Pore Formation

1. Introduction

Laser Additive Manufacturing (LAM) is a highly versatile and flexible manufacturing technology, enabling layer-by-layer fabrication of complex components. Directed Energy Deposition (DED-AM)[1] using blown-powder and a laser heat source is commonly used to fabricate[2], repair[3] or add additional material to existing components[4]. However, potentially detrimental features such as lack of fusion, balling and high surface roughness are found to be difficult to eliminate in blown-powder DED-AM titanium alloy builds[5]. Although there have been many studies undertaken to improve the process, there has been only limited progress due to the lack of fundamental understanding of the underlying physics governing deposition. The detrimental features can compromise the structural integrity[6] and restrict the use of parts in safety-critical applications. Traditional *ex situ* microstructural characterisation of deposits[7–9] and measurement of bulk mechanical properties[10–13] provides valuable information but can be inefficient in the use of materials and time. Moreover, it does not reveal the transient dynamics of phenomena underpinning the restraints on the utilisation of laser-based blown-powder DED-AM.

Titanium alloys are some of the most widely used materials in LAM due to their good mechanical performance in aerospace, automotive and biomedical applications[14,15]. The titanium alloy Ti-6Al-2Sn-4Zr-2Mo (in wt%) (Ti6242) is a near-α titanium alloy composition that combines good toughness, high temperature stability and good creep resistance. It is typically used for structural components at elevated temperatures in power generation and aeroengine

gas turbines [16]. It has mechanical properties that are superior to the properties of the traditional Ti-6wt%Al-4wt%V at elevated temperatures and is thus an alloy which is of particular interest in the aerospace industry. For this reason the present *in situ* synchrotron X-ray imaging study focused on producing an improved understanding of blown-powder DED-AM with a laser heat source to reveal the underlying physics controlling build features at both the macro- and micro-structural levels and to elucidate the effect of processing conditions on powder deposition characteristics.

In situ and *operando*, high-speed X-ray imaging and diffraction investigations of laser powder bed fusion (LPBF), [17–22] have been able to capture dynamic phenomena in the molten pool, including melt flow[18,23], defect formation[20,24], together with phase and strain evolution[25]. To date, less attention has been given to blown-powder DED-AM due to the challenge of the larger thickness of the deposited bead, leading to reduced X-ray transmission. However, high-flux, high energy third-generation synchrotron radiation sources[26] render the observation of the phenomena occurring on the time and length scales associated with blown-powder DED-AM[27,28] accessible. Wolff *et al.* [24] pioneered the *in situ* observation of the blown powder process using a piezo-driven powder delivery system to meter a flow of powder particles from a syringe-needle falling under gravity. More recently Chen *et al*. [27,29,30] successfully captured the laser-matter interaction of a blown-powder AM process at a near-industrial scale and elucidated the extent to which behaviour is materials-dependent, illustrating the potential industrial benefits of *in situ* observation.

This work reported in this paper was undertaken in order to study the process of blown-powder DED AM with a laser heat source of Ti-6242 *in situ* and *operando* using synchrotron X-ray imaging. Using different build strategies, we were able to observe single track deposit evolution, melt pool morphology and multilayer build phenomena. We were able to observe a unique melt pool morphology occurring with Ti6242 and to gain an increased understanding of gas pore formation and dynamics. The results presented in this work enhance our fundamental understanding of DED-AM processing.

2. Methods

2.1 DED-AM: Blown Powder Additive Manufacturing Process Replicator

In order to replicate a commercial laser DED-AM system for use on synchrotron beamlines (e.g. theI12: the Joint Engineering, Environmental, and Processing (JEEP) at Diamond Light Source[31]) a blown powder additive manufacturing process replicator (BAMPR) was developed. The system employs a stationary laser beam and powder feeder. The substrate which is ~ 1mm wide moves at a pre-determined traverse speed. The laser power (P) is comparatively low [29] (100-300 W) in order to generate a melt pool that allows sufficient transmission of the X-ray beam for imaging. However, a small beam diameter ensures that the BAMPR uses a laser power density which is relevant to industrial practice. Details of the apparatus, including the powder delivery system, can be found in references [27,29,30]. A schematic diagram of the setup and details of the deposition parameters used in the present study are provided in the supplementary information. Gas atomised Ti-6242 powder with a spherical particle morphology, size range of 45 - 90 μm and a median particle size (D_{50} of 70 μm) was used. The first layer was deposited onto a substrate of Ti-6242.

2.2 Synchrotron radiography, image processing and feature quantification

A monochromatic X-ray beam with a mean X-ray energy of approximately 53 keV was used throughout all the imaging experiments performed in this study. The synchrotron X-ray beam is selectively attenuated by passing through the sample and impinges on scintillator screen. X-rays are then re-emitted as visible light by the scintillator and unless otherwise stated were captured by a high-speed camera (PCO.edge). A framerate of 200 frames per second and a pixel size of 3.24 μm were selected as the optimal parameters for a high signal to noise ratio (S/N) image whilst still capturing melt pool features and pore formation in the melt pool. A dark-field correction is applied internally on the camera during image acquisition. Subsequently, all the acquired radiographs were processed using both ImageJ[32] and Matlab. A flat-field correction (FFC) was applied through a pixelwise division by a mean of 100

flat-field images[18] to remove artefacts and noise variation inherited during the acquisition process . To reveal features unique to a given frame a local-temporal background subtraction (LTBS) is applied using:

$$\mathrm{LTBS} = \frac{FFC}{I_{lavg}}$$

Where, I_{lavg} is a local average of 50 of the nearest neighbour images.

The melt tracks were examined post-build by XCT using a Nikon XTH225 (Nikon, Japan) to image the interior features and powder particles attached to the melt tracks.

3. Results & Discussion

3.1 In situ observation of melt track initiation during DED-AM of Ti6242

To reveal the mechanisms governing melt track initiation for Ti-6242 powder DED-AM, the onset of a melt track with powder deposition was captured at a laser power (P) of 200 W, powder feed rate (F) of 1 g/min and substrate traverse speed (v) of 1 mm/s. Figure 1 shows images captured 0.3 and 0.7 s after the laser was turned on. The build-up of a deposit can be clearly observed to be related to surface melting and is revealed more clearly in Supplementary Video 1. Powder particles first coalesced onto the melted substrate plate approximately 0.3 s after the laser was turned on and formed a melt pool. With the traverse of the substrate plate, powder particles were continuously incorporated into the melt pool, resulting in the formation of a deposit. The melt track initiation in Ti6242, via laser surface melting, is similar to that seen in stainless steel[29]. An approximately semi-circular molten pool in the substrate can be observed in the projection radiographs and indicates that the laser melting process was conduction mode[33] rather than keyhole mode[34]. Video 1 illustrates clearly that powder particles stick to the molten surface (they rebound prior to the onset of melting), melt and spread across the substrate; probably this is driven by surface tension and capillary forces. Interestingly, we observed particles deposited at the edge of the melt pool at 0.7 s, which were not melted but appeared to adhere and accumulate on the surface; these

have the appearance of being sintered. Such particles were more apparent during multi-layer deposition (section 3.3) and their features are discussed more fully in that section. It is notable that this sintered powder phenomenon was not observed during deposition of stainless steel[30]which was deposited using the same powder feeder and laser beam diameter. It is thus hypothesised that whilst the mismatch of the laser beam diameter and the (larger) powder feeder focal diameter is a cause of the over spray outside the melt pool, the sintering effect appears to be a material dependent phenomenon.

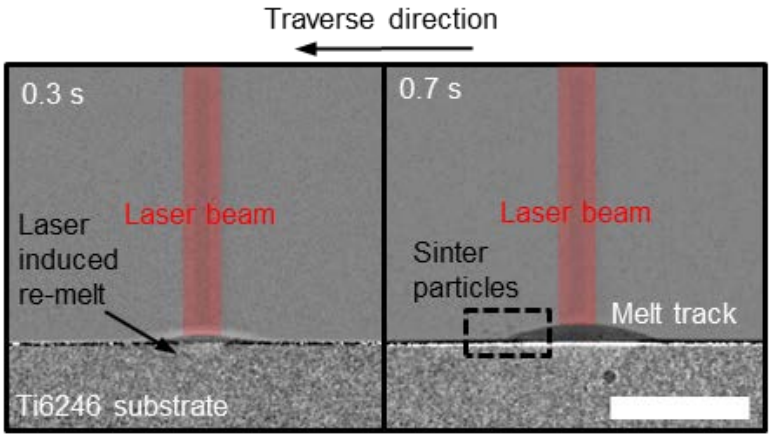

Figure 1. Local-temporal background subtraction radiographs acquired during DED revealing the melt track initiation mechanism under P = 200 W, v = 1 mm/s, F= 1 g/min. The sintered particles can be observed to accumulate at the edge of the melt track in Supplementary Video 1. Scale bar = 1000 µm. Time zero is when the laser was switched on. Captured at 5kfps using a MIRO 310M (Vision Research Inc.) with a pixel size of 6.67 µm.

3.2 Quantification of the melt pool dimensions in the first layer

The dimensions of the melt pool depend on laser power (P), traverse speed (v) and also on the mass flow rate of powder (F) because it absorbs the incident laser beam energy and affects the thermal gradient within the melt pool[35]. Figure 2 shows the length, depth and apparent melt pool volume, as a function of F, P and v, with representative radiographs inset. The melt pool volume was determined by assuming it to adopt a spherical-cap shape. The apparent melt pool volume was calculated from the characteristic dimensions as described in

Supplementary Information. It should be noted that these characteristic dimensions are extracted from the innermost phase contrast fringe outlining the solid-liquid boundary [36]. As such, the apparent volumes shown in Figure 2 are likely to be underestimates of the true melt pool volume.

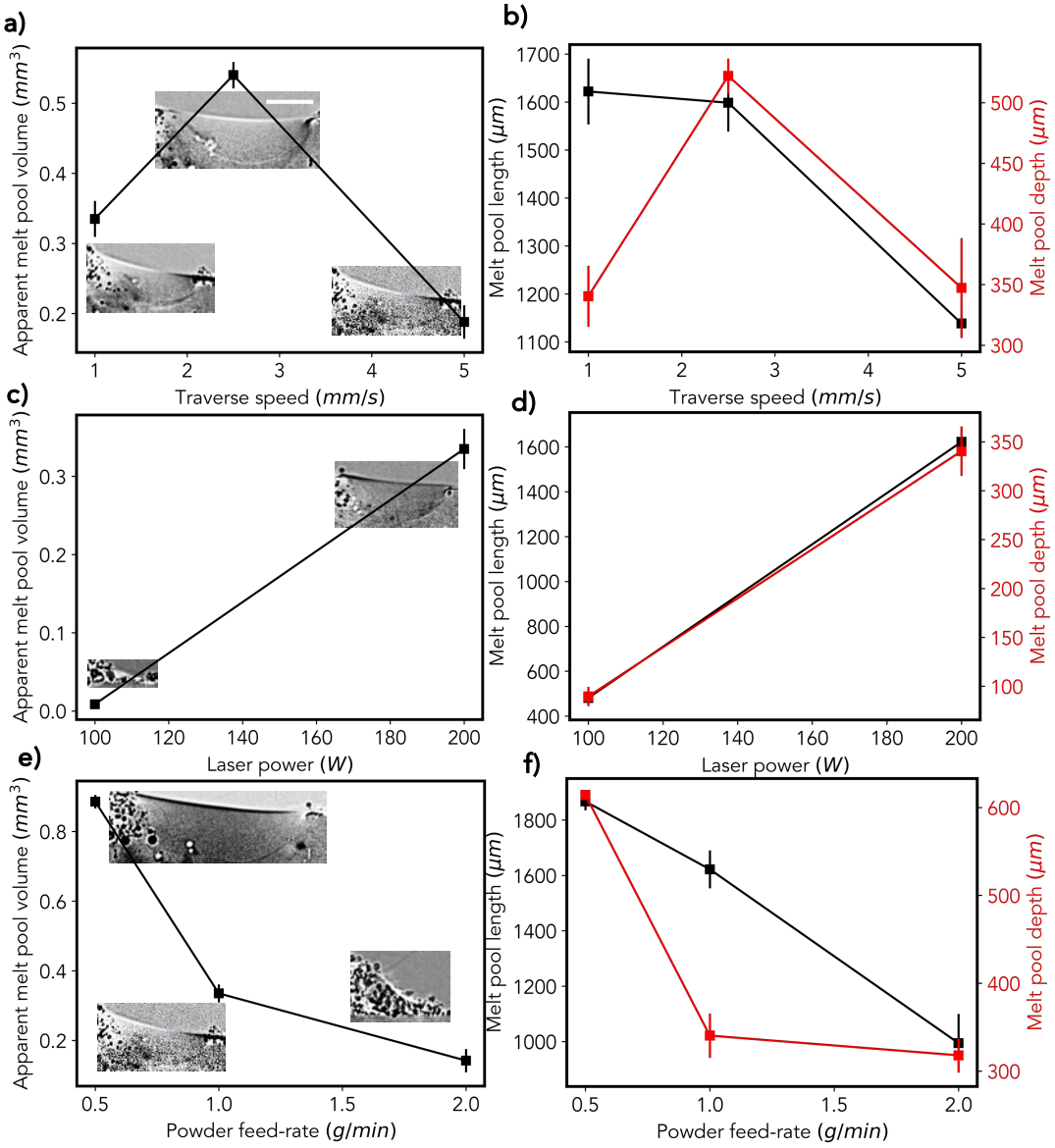

Figure 2. Plots of apparent melt pool volume, length and depth versus powder feed-rate, laser power and traverse speed. Error bars indicate the standard deviation of the measurements. (a) & (b) dimension versus traverse speed, v, at 1 g/min and 200 W; (c) & (d) dimension versus laser power, P, at 1 g/min and 1 mm/s; (e) & (f) dimension versus powder feed rate, F, at 1 mm/s and 200 W. Scale bar = 500 µm. Insets show representative radiographs of melt pools.

158 The apparent melt pool volume and profile both increase with increasing laser power,
159 illustrating that the best build occurs when there is sufficient power density to enable all powder
160 deposited into the melt-pool to be melted. Conversely, with increasing powder feed-rate, the
161 apparent melt pool volume decreases, as more energy goes into melting the powder. There
162 is a sharper decrease in melt pool depth than the length with increasing feed rate, perhaps
163 due to the known scattering of the incident laser beam [37]; the powder stream effectively
164 scatters the laser reducing the energy delivered to the melt pool. In our experiment, this
165 phenomenon shows that with twice the mass of powder added as the feed rate is increased
166 from 0.5 to 1 g/min, more energy goes to melting the powder and less to re-melting the track
167 below. This would produce a cooler, shallower pool. With increasing traverse speed added
168 material and the added heat (both on a per unit length basis) are reduced. At the slowest
169 speed, 5 times the amount of heated powder is deposited around the pool per unit length. This
170 additional sinter builds a wall changing the apparent weld pool shape to a saddle, as discussed
171 later. However, increasing the traverse speed decreases both the laser energy per unit length
172 and the amount of powder depositing into the melt pool, and the melt pool volume decreases
173 accordingly.

174 *3.3 In situ observation of the development of multi-layer melt-tracks*

175 The morphological evolution of Ti-6242 tracks with different traverse speeds and laser powers
176 captured by X-ray imaging is shown in Figure 3, Figure 4, and Supplementary Videos 2 to 7.
177 All builds were 5 layers in height and performed using a bi-directional strategy with feedrate
178 at 1 g/min.

179 Figure 3 shows radiographs captured at 200 W and a range of traverse speeds. On the first
180 layer, the laser beam is observed to melt the substrate surface which then subsequently
181 consolidates impinging powder particles resulting in the formation a continuous melt track.
182 Unmelted powder particles also adhere to the periphery of the melt-pool at the build start and,
183 as the substrate moves, these adhered particles cover the newly formed track. This layer of

184 powder was examined *ex situ* in a scanning electron microscope (SEM) and an X-ray
185 computed tomography (XCT). The particles appear to comprise both partially melted particles
186 and particles that are joined by necks, a feature consistent with solid state sintering. SEM
187 images are shown in the Supplementary information. Sintered particles appear to occur with
188 higher frequency and so in this paper the accumulation is referred to as a sintered layer.

189 The thickness of this sintered particle layer directly correlates with the substrate traverse
190 speed, Figure 3. This would be expected because the laser parameters are fixed and thus for
191 a given powder mass flow rate a reduction in the traverse speed increases the mass deposited
192 per unit length of track. Sintered particles were observed around the melt pool. These particles
193 may have been sintered by high-temperature solid-state diffusion aided by laser heating,
194 forming necks [38]. The thick sinter layers formed at low traverse speeds causes lack of fusion
195 features and increases surface roughness. At 1 mm/s, it is seen in Figure 3 that the 5th layer
196 has developed a thick covering of sinter and this is seen to be a probable cause for regions of
197 lack of fusion between layers 4 and 5.

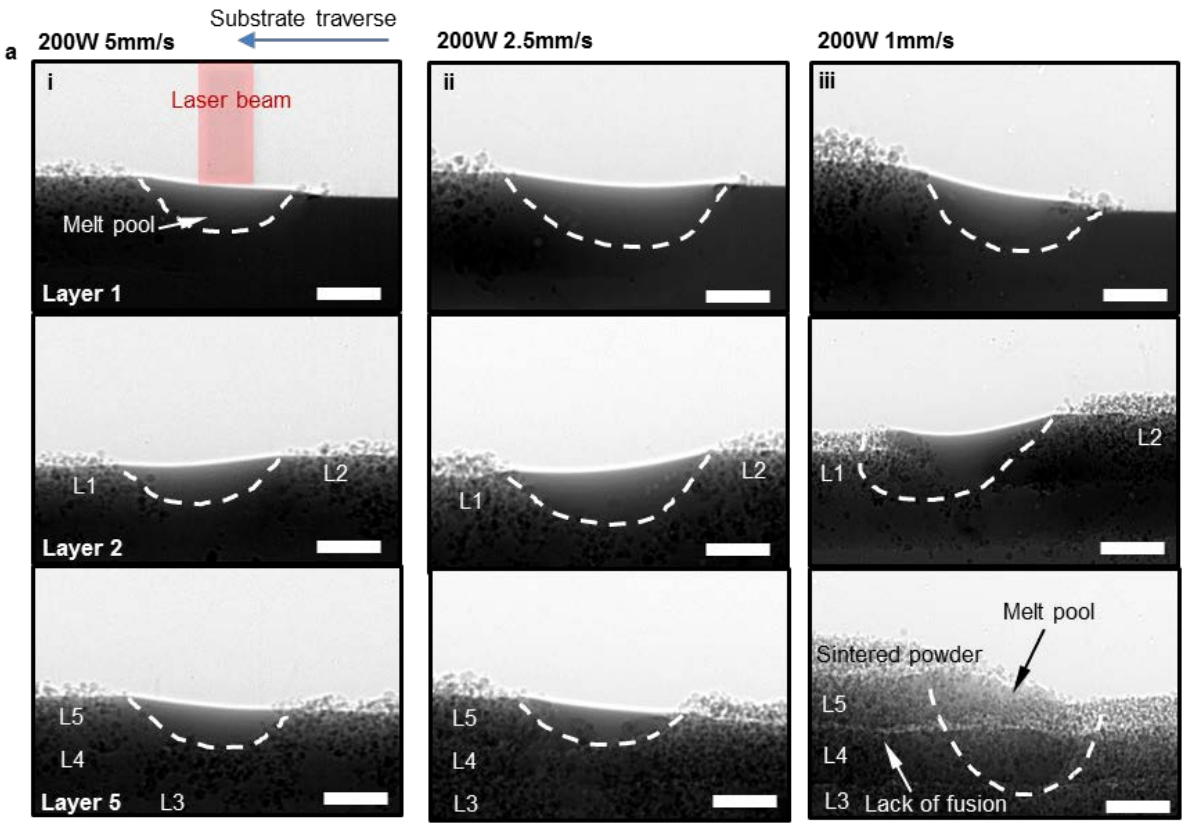

198

Figure 3. Multi-layer melt track morphologies. Representative radiographs of powder DED AM Ti-6242, showing the variation in melt pool and track morphologies with different substrate traverse speeds and a laser power of 200 W, a powder feedrate of 1 g/min. See Supplementary Videos 2-4. Scale bar = 500 µm. Note that substrate traverse direction is reversed for layer 2.

Figure 4 differs from Figure 3 in that it shows the behaviour at the same traverse speeds when the laser power was decreased to 100 W. A main feature is that the amount of fully dense track relative to the amount of sintered powder is seen to be significantly reduced.

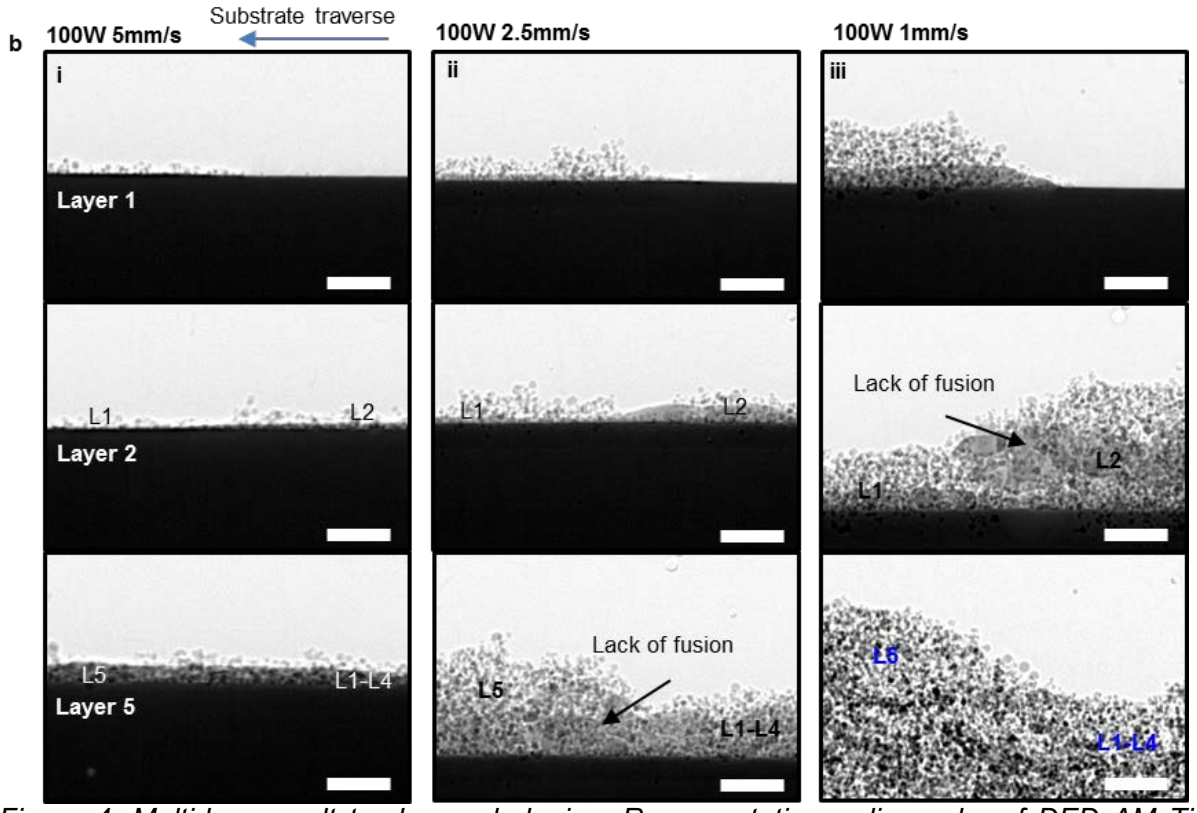

Figure 4. Multi-layer melt track morphologies. Representative radiographs of DED AM Ti-6242, showing the variation in melt pool and track morphology with different substrate traverse speeds and a laser power of 100 W, a powder feedrate of 1 g/min. Melt pool boundary is not visible due to low energy density. See Supplementary Videos 5-7. Scale bar = 500 µm. Note that substrate traverse direction is reversed for layer 2.

3.4 Observations on melt pool morphology in multilayer builds

Utilising a local-temporal background subtraction (LTBS), the melt pool morphology was revealed in Figure 5(a). The projected melt pool area is delineated by the phase contrast fringes generated by the solid-liquid boundary. Using these fringes, a double melt pool can be observed and pores can be seen hovering at multiple locations within the pool. In the cross-sectional view of the post-mortem XCT scan (Figure 5b), a concave or saddle-shaped pool is visible. This observation is in accordance with the observations of Gharbi *et al.*[39,40] who attributed the formation of the concave melt pool in Ti-6Al-4V to radially outward Marangoni flow. Similarly, in Ti6242 a concave melt pool is evident from the micrographs presented by Richter *et al*. [41]. A 3D schematic (Figure 5b) of the concave melt pool is developed based on the observations.

The concave melt pool additionally poses challenges in melt pool volume calculation from the X-ray radiographs as a simple relationship between the observed boundary in the radiograph can no longer be assumed. The melt pool geometry measurements reported in Section **3.3** used the smaller portion of the melt pool as it is suggested this more reliably represents the volume through-thickness.

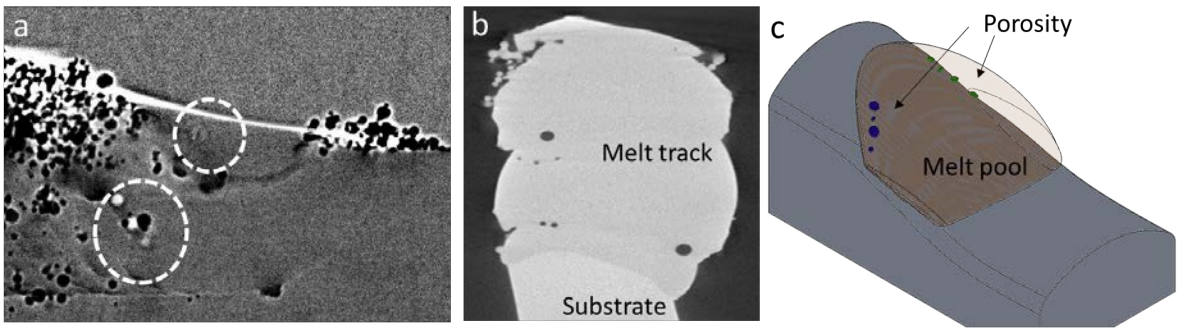

Figure 5. Melt pool morphology of Ti-6242 during DED-AM. A substrate traverse speed of 1 mm/s, a laser power of 200 W, and a powder feedrate of 1 g/min was used. (a) a local-temporal background subtraction processed radiograph showing the boundary of the saddle-shaped melt pool and the pores inside the pool. Scale bar = 500 µm. See Supplementary Video 10. (b) Corresponding post-mortem xCT cross-section shows the concave shape of the bottom of the melt pool. Scale bar = 1 mm. (c) 3D schematic of the melt pool showing the saddle-shaped

melt pool under X-ray imaging is due to the concave shape. The pores in the saddle-shaped melt pool are sitting on the two edges of the concave melt pool edge (see final positions in (a)). Scale bar = 1 mm.

3.5 Mechanisms of pore evolution in the melt pool

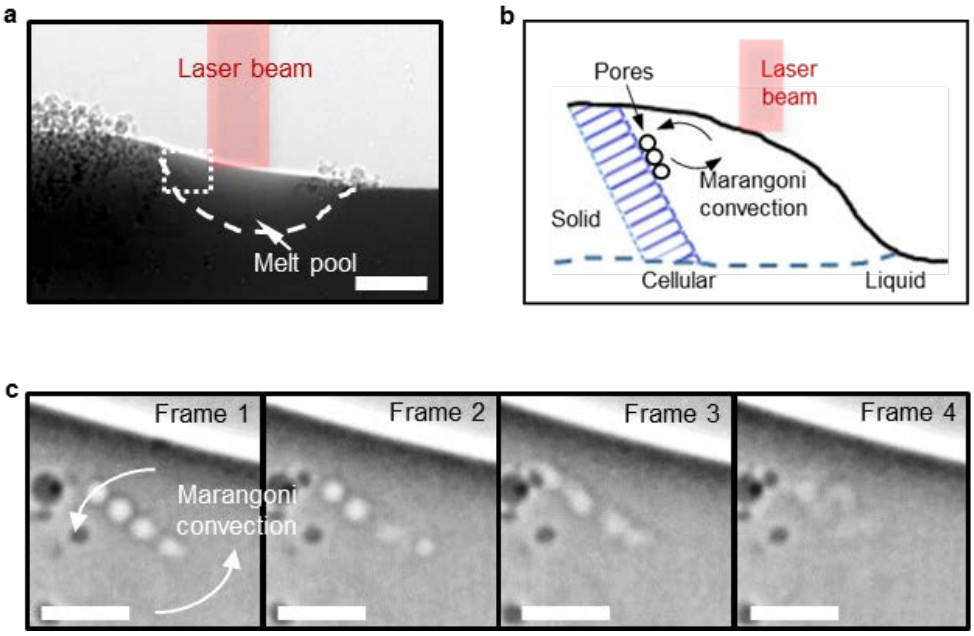

Figure 6. Understanding pore formation during DED-AM of Ti-6242. (a) Radiograph of a single layer track revealing pore pushing phenomenon. (b). Schematic of pore pushing mechanism in DED-AM build using Ti-6242. (c) Enlarged time series radiographs of the boxed area in (a) showing pores swirling with Marangoni convection at the back of the melt pool, see Supplementary video 2. Scale bar = 250 µm.

During the Ti-6242 AM build process, we captured the formation of porosity, see Supplementary video 2. The results of the present study show that pores form in the melt pool which have predominantly circular cross-section in radiographs and are thus presumed to be approximately spherical. These are likely to be gas induced pores because the process operates in conduction mode with a stable melt pool and not keyhole mode where melt pool instabilities can drive pore formation.

One source of gas in the system is argon which occurs as residual pores within titanium alloy powder feedstock[42]. It is also possible that a gas that is soluble in titanium alloys, such as hydrogen, can be absorbed into the melt pool from the decomposition of moisture in the process chamber environment and potentially also from the surface of the powder. Hydrogen has been shown to cause porosity in titanium alloy welds [79–81], where at the liquidus temperature hydrogen is twice as soluble in the liquid as the solid (partition coefficient of ca. 0.5 [82]). Hence, hydrogen is rejected into the melt pool by the advancing solid-liquid interface and the melt becomes supersaturated there. This can potentially lead to pore nucleation in the melt as proposed in [43].

A further consideration is then whether a gas pore can rise to the surface and escape from the melt pool and this will depend on many factors including the fluid dynamic forces that are acting on it. Fluid flow in the molten pool is primarily caused by the combined effects of Marangoni and buoyancy forces and the momentum due to the impingement of powder particles onto the melt pool. The radiographs reveal that not all gas pores rise rapidly to the surface and escape from the melt pool but some are pushed along by the solid-liquid interface and thus appear to accumulate at the end of the deposit track. It is notable that a similar effect has been noted during both LPBF and EBPBF [44,45] of the alloy Ti6Al4V.

The interaction between pores and a solid-liquid solidification front is not well understood. To explore this further we have calculated a microstructure selection map for Ti6242 using the methodology set out in the Supplementary Information.

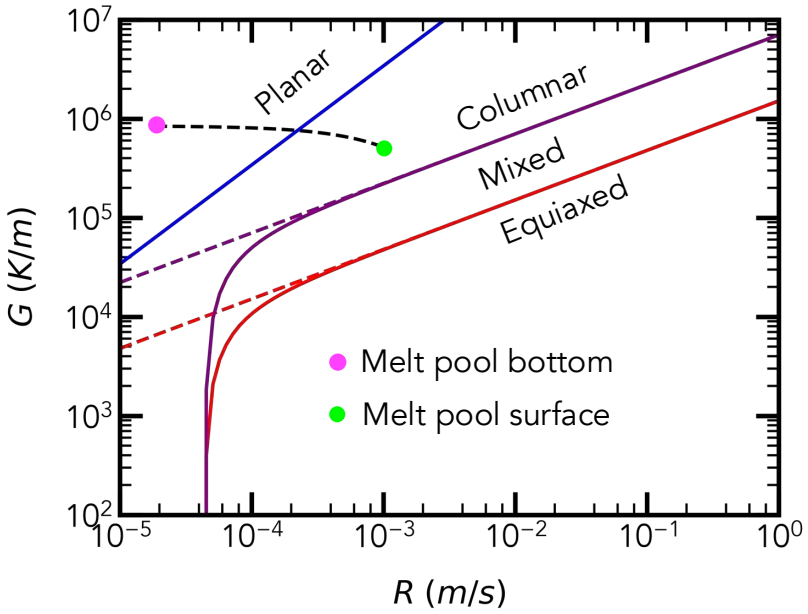

271

272 *Figure 7. Grain structure selection map*

273 The map derived from this analysis shows (Figure 7) the estimated constitutional supercooling
274 (CS) criterion for planar front growth of Ti6242 superimposed onto the well-established grain
275 structure selection map for columnar or equiaxed growth developed by Kobryn and
276 Semiatin[46]. It is assumed that the present alloy, Ti6242, behaves in a similar manner to Ti-
277 6Al-4V for which Kobryn's map was determined.

278 In Figure 7 the dashed line black line indicates the calculated variation in G and R along the
279 solidification front isotherm for 1 mm s^{-1}, 200 W, process conditions in the present study.
280 Therefore, at the bottom of the melt-pool an initially planar solidification front is expected but
281 closer to the melt pool surface (within ~750 mm of the surface) a cellular-dendritic front is
282 expected which will transition to one of increasingly dendritic character closer to the surface
283 as G/R decreases. The G and R values obtained from the present analysis are not dissimilar
284 to those reported by Bontha et al[47]. for the columnar dendritic growth found in laser blown
285 powder DED of Ti-6Al-4V. Their analysis indicates R~$3x10^{-3}$ ms^{-1} and G~$3x10^{6}$ Km^{-1} for a
286 laser energy density of ~ 150 J/mm as compared with the present energy density of 200 J/mm
287 which is towards the higher end of energy density used in blown powder DED [48].

Therefore, it can be concluded that, given the conditions are not far removed from the CS planar front stability criterion, it is most likely the pores seen in Figure 6 are being pushed along by a cellular or cellular dendritic front.

The physics underlying pushing or capture of gas pores is complex and is believed to depend on various pore and metal properties as well as the fluid flow characteristics of the pool[49]. Specifically, little appears to be known about the effect of solidification rate or solidification front morphology on whether capture or pushing takes place. Although not specifically concerned with gas pores, Han and Hunt [50] have studied a similar phenomenon namely the interaction between non-metallic particles and a solidification front.

They proposed that pushing of particles/pores ahead of a solidification front could occur if the pore is moved over the interface by fluid flow. They suggested that such a mechanism could be valid in the case of a planar front or one where the pore size is large in comparison with the cell spacing. We suggest therefore that this mechanism could well be responsible for the present observations on pore pushing. The Marangoni and other convective flows in the melt pool could ensure motion of the gas pores over the solidification front. Moreover, it is evident that pore sizes are likely to be larger that cell spacing during DED-AM. The high cooling rates of the process of 10^3 to 10^4 K/s are likely to promote cell or primary dendrite arm spacings that are in the range 1-10 μm [48].

We hypothesise that the pore is not engulfed at the solidification front due to the interface predominantly exhibiting a cellular solidification mode, commonly observed during the DED of titanium alloys [47]. The columnar cellular solidification front (which cannot be resolved in the present experiments and is not preserved to room temperature due to the solid-state phase transformation effectively prevents the pores from being engulfed into the solidifying track and instead results in pore pushing. The pores are thus swept along with the melt-pool at its back wall of the pool (Figure 3(b) and (c) and Supplementary video 2). Similar behaviour has been observed and theoretically explained during the welding on Nickel-Copper alloys [43].

4. Conclusions

In situ and *operando* synchrotron X-rays were used to understand the Directed Energy Deposition Additive Manufacturing (DED-AM) process of Ti-6242 using a custom-built apparatus known as a blown powder AM process replicator (BAMPR). The radiographs revealed key laser-matter interaction and powder consolidation mechanisms during the manufacturing process of Ti-6242, including:

- *Sintering*: The sintering of powder particles, particularly at low substrate traverse speeds has been reported. Powder particles are suggested to have been sintered by high-temperature solid-state diffusion aided by laser heating, forming necks. The thick sinter layers formed at low traverse speeds causes lack of fusion features and surface roughness.
- *Melt pool morphology*: The melt pool shows a concave (or saddle) shape, revealed by a double melt pool in radiographs.
- *Porosity*: The pushing of gas porosity at the solidification front was observed. Analysis using a heat flow model based upon the Rosenthal 2D line source model, combined with an experimental microstructure selection map, allows us to propose that the solidifying interface is likely to be cellular/cellular-dendritic in nature. It is suggested that this solidification front, , combined with fluid flow in the melt pool, effectively prevents the pores from being engulfed into the solid and instead results in pore pushing.

The findings presented in this study enhance the understanding of DED-AM processes in Ti-alloys and are envisaged to act as guidance for best manufacturing practice.

Acknowledgements

We acknowledge the Research Complex at Harwell for use of facilities and thank the Diamond Light Source (DLS) for providing the beamtime at beamline I12: JEEP (MT20096). This

research was supported under MAPP: EPSRC Future Manufacturing Hub Manufacture using Advanced Powder Processes (EP/P006566/1), a Royal Academy of Engineering Chair in Emerging Technology (CiET1819/10), and Rolls-Royce plc. via the Horizon 2020 Clean Sky 2 WP5.8.1 programs and through the support of L.S.'s studentship. S.C. was supported by the Office for Naval Research under grant number N62909-19-1-2109. The authors are grateful to Prof Graham McCartney for valuable discussions on solidification features. The provision of materials and technical support from Rolls-Royce plc is gratefully acknowledged.

Author contributions

P.D.L. conceived the project. Y.C., S.C. and S.M., led the design of the Blown Powder Additive Manufacturing Process Replicator (BAMPR). Y.C. and S.C. designed and performed the experiments, with all authors contributing. Y.C. performed the data analysis with S.C. contributing. Y.C., P.D.L. and S.C. led the results interpretation and paper writing, with all authors contributing.

References

[1] T. DebRoy, H.L. Wei, J.S. Zuback, T. Mukherjee, J.W. Elmer, J.O. Milewski, A.M. Beese, A. Wilson-Heid, A. De, W. Zhang, Additive manufacturing of metallic components – Process, structure and properties, Prog. Mater. Sci. 92 (2018) 112–224. doi:10.1016/j.pmatsci.2017.10.001.

[2] A. Saboori, A. Aversa, G. Marchese, S. Biamino, M. Lombardi, P. Fino, Application of directed energy deposition-based additive manufacturing in repair, Appl. Sci. 9 (2019). doi:10.3390/app9163316.

[3] M. Leino, J. Pekkarinen, R. Soukka, The role of laser additive manufacturing methods of metals in repair, refurbishment and remanufacturing - Enabling circular economy, Phys. Procedia. 83 (2016) 752–760. doi:10.1016/j.phpro.2016.08.077.

[4] A. Panesar, I. Ashcroft, D. Brackett, R. Wildman, R. Hague, Design framework for multifunctional additive manufacturing: Coupled optimization strategy for structures with embedded functional systems, Addit. Manuf. 16 (2017) 98–106. doi:10.1016/J.ADDMA.2017.05.009.

[5] S. Liu, Y.C. Shin, Additive manufacturing of Ti6Al4V alloy: A review, Mater. Des. 164 (2019) 107552. doi:https://doi.org/10.1016/j.matdes.2018.107552.

[6] S.M.J. Razavi, G.G. Bordonaro, P. Ferro, J. Torgersen, F. Berto, Fatigue Behavior of Porous Ti-6Al-4V Made by Laser-Engineered Net Shaping, Mater. (Basel, Switzerland). 11 (2018). doi:10.3390/ma11020284.

[7] F. Yan, W. Xiong, E.J. Faierson, Grain structure control of additively manufactured metallic materials, Materials (Basel). 10 (2017) 1260. doi:10.3390/ma10111260.

[8] C. Kumara, A. Segerstark, F. Hanning, N. Dixit, S. Joshi, J. Moverare, P. Nylén, Microstructure modelling of laser metal powder directed energy deposition of alloy 718, Addit. Manuf. 25 (2019) 357–364. doi:10.1016/J.ADDMA.2018.11.024.

[9] N.A. Kistler, D.J. Corbin, A.R. Nassar, E.W. Reutzel, A.M. Beese, Effect of processing conditions on the microstructure, porosity, and mechanical properties of Ti-6Al-4V repair fabricated by directed energy deposition, J. Mater. Process. Technol. 264 (2019) 172–181. doi:10.1016/J.JMATPROTEC.2018.08.041.

[10] S. Leuders, M. Thöne, a. Riemer, T. Niendorf, T. Tröster, H. a. Richard, H.J. Maier, On the mechanical behaviour of titanium alloy TiAl6V4 manufactured by selective laser melting: Fatigue resistance and crack growth performance, Int. J. Fatigue. 48 (2013) 300–307. doi:10.1016/j.ijfatigue.2012.11.011.

[11] N. Shamsaei, J. Simsiriwong, Fatigue behaviour of additively-manufactured metallic parts, Procedia Struct. Integr. 7 (2017) 3–10. doi:10.1016/J.PROSTR.2017.11.053.

[12] A. Alafaghani, A. Qattawi, M.A.G. Castañón, Effect of manufacturing parameters on the microstructure and mechanical properties of metal laser sintering parts of precipitate hardenable metals, Int. J. Adv. Manuf. Technol. 99 (2018) 2491–2507. doi:10.1007/s00170-018-2586-5.

[13] A. Arifin, A.B. Sulong, N. Muhamad, J. Syarif, M.I. Ramli, Material processing of hydroxyapatite and titanium alloy (HA/Ti) composite as implant materials using powder metallurgy: A review, Mater. Des. 55 (2014) 165–175. doi:10.1016/j.matdes.2013.09.045.

[14] Z. Zhang, D. Jones, S. Yue, P.D. Lee, J.R. Jones, C.J. Sutcliffe, E. Jones, Hierarchical tailoring of strut architecture to control permeability of additive manufactured titanium implants, Mater. Sci. Eng. C. 33 (2013) 4055–4062. doi:https://doi.org/10.1016/j.msec.2013.05.050.

[15] T.B. Kim, S. Yue, Z. Zhang, E. Jones, J.R. Jones, P.D. Lee, Additive manufactured porous titanium structures: Through-process quantification of pore and strut networks, J. Mater. Process. Technol. 214 (2014) 2706–2715. doi:10.1016/j.jmatprotec.2014.05.006.

[16] A. Chamanfar, T. Pasang, A. Ventura, W.Z. Misiolek, Mechanical properties and microstructure of laser welded Ti–6Al–2Sn–4Zr–2Mo (Ti6242) titanium alloy, Mater. Sci. Eng. A. 663 (2016) 213–224. doi:https://doi.org/10.1016/j.msea.2016.02.068.

[17] C. Zhao, K. Fezzaa, R.W. Cunningham, H. Wen, F. De Carlo, L. Chen, A.D. Rollett, T. Sun, Real-time monitoring of laser powder bed fusion process using high-speed X-ray imaging and diffraction, Sci. Rep. 7 (2017) 3602. doi:10.1038/s41598-017-03761-2.

[18] C.L.A. Leung, S. Marussi, R.C. Atwood, M. Towrie, P.J. Withers, P.D. Lee, In situ X-ray imaging of defect and molten pool dynamics in laser additive manufacturing, Nat. Commun. 9 (2018) 1–9. doi:10.1038/s41467-018-03734-7.

[19] N.P. Calta, J. Wang, A.M. Kiss, A.A. Martin, P.J. Depond, G.M. Guss, V. Thampy, A.Y. Fong, J.N. Weker, K.H. Stone, C.J. Tassone, M.J. Kramer, M.F. Toney, A. Van Buuren, M.J. Matthews, An instrument for in situ time-resolved X-ray imaging and diffraction of laser powder bed fusion additive manufacturing processes, Rev. Sci. Instrum. 89 (2018). doi:10.1063/1.5017236.

[20] A.A. Martin, N.P. Calta, J.A. Hammons, S.A. Khairallah, M.H. Nielsen, R.M. Shuttlesworth, N. Sinclair, M.J. Matthews, J.R. Jeffries, T.M. Willey, J.R.I. Lee, Ultrafast dynamics of laser-metal interactions in additive manufacturing alloys captured by in situ X-ray imaging, Mater. Today Adv. 1 (2019) 100002. doi:10.1016/J.MTADV.2019.01.001.

[21] M. Álvarez-Murga, J.P. Perrillat, Y. Le Godec, F. Bergame, J. Philippe, A. King, N. Guignot, M. Mezouar, J.L. Hodeau, Development of synchrotron X-ray micro-tomography under extreme conditions of pressure and temperature, J. Synchrotron Radiat. 24 (2017) 240–247. doi:10.1107/S1600577516016623.

[22] Y. Miao, T. Yao, J. Lian, J.S. Park, J. Almer, S. Bhattacharya, A.M. Yacout, K. Mo, In situ synchrotron investigation of grain growth behavior of nano-grained UO2, Scr. Mater. 131 (2017) 29–32. doi:10.1016/j.scriptamat.2016.12.025.

[23] R. Cunningham, C. Zhao, N. Parab, C. Kantzos, Keyhole threshold and morphology in laser melting revealed by ultrahigh-speed x-ray imaging, 852 (2019) 849–852.

[24] S.J. Wolff, H. Wu, N. Parab, C. Zhao, K.F. Ehmann, T. Sun, J. Cao, In-situ high-speed X-ray imaging of piezo-driven directed energy deposition additive manufacturing, Sci. Rep. 9 (2019) 1–14. doi:10.1038/s41598-018-36678-5.

[25] P. Raterron, S. Merkel, In situ rheological measurements at extreme pressure and temperature using synchrotron X-ray diffraction and radiography, J. Synchrotron Radiat. 16 (2009) 748–756. doi:10.1107/S0909049509034426.

[26] M. Drakopoulos, T. Connolley, C. Reinhard, R. Atwood, O. Magdysyuk, N. Vo, M. Hart, L. Connor, B. Humphreys, G. Howell, S. Davies, T. Hill, G. Wilkin, U. Pedersen, A. Foster, N. De Maio, M. Basham, F. Yuan, K. Wanelik, I12: the Joint Engineering, Environment and Processing (JEEP) beamline at Diamond Light Source, J. Synchrotron Radiat. 22 (2015) 828–838. doi:10.1107/S1600577515003513.

[27] Y. Chen, S. Clark, A.C.L. Leung, L. Sinclair, S. Marussi, R. Atwood, T. Connoley, M. Jones, G. Baxter, P.D. Lee, Melt pool morphology in directed energy deposition additive manufacturing process, IOP Conf. Ser. Mater. Sci. Eng. 861 (2020) 012012. doi:10.1088/1757-899x/861/1/012012.

[28] S.J. Clark, C.L.A. Leung, Y. Chen, L. Sinclair, S. Marussi, P.D. Lee, Capturing Marangoni flow via synchrotron imaging of selective laser melting Capturing Marangoni flow via synchrotron imaging of selective laser melting, (2020). doi:10.1088/1757-899X/861/1/012010.

[29] Y. Chen, S.J. Clark, L. Sinclair, C.L.A. Leung, S. Marussi, T. Connolley, O. V. Magdysyuk, R.C. Atwood, G.J. Baxter, M.A. Jones, D.G. McCartney, I. Todd, P.D. Lee, In situ and Operando X-ray Imaging of Directed Energy Deposition Additive Manufacturing, ArXiv. (2020) 1–31. http://arxiv.org/abs/2006.09087.

[30] Y. Chen, S.J. Clark, Y. Huang, L. Sinclair, C. Lun Alex Leung, S. Marussi, T. Connolley, O. V. Magdysyuk, R.C. Atwood, G.J. Baxter, M.A. Jones, I. Todd, P.D. Lee, In situ X-ray quantification of melt pool behaviour during directed energy deposition additive manufacturing of stainless steel, Mater. Lett. 286 (2021) 129205. doi:10.1016/j.matlet.2020.129205.

[31] M. Drakopoulos, T. Connolley, C. Reinhard, R. Atwood, O. Magdysyuk, N. Vo, M. Hart, L. Connor, B. Humphreys, G. Howell, S. Davies, T. Hill, G. Wilkin, U. Pedersen, A. Foster, N. De Maio, M. Basham, F. Yuan, K. Wanelik, I12: The Joint Engineering,

462 Environment and Processing (JEEP) beamline at Diamond Light Source, J.
463 Synchrotron Radiat. 22 (2015) 828–838. doi:10.1107/S1600577515003513.

464 [32] J. Schindelin, I. Arganda-Carreras, E. Frise, V. Kaynig, M. Longair, T. Pietzsch, S.
465 Preibisch, C. Rueden, S. Saalfeld, B. Schmid, J.-Y. Tinevez, D.J. White, V.
466 Hartenstein, K. Eliceiri, P. Tomancak, A. Cardona, Fiji: an open-source platform for
467 biological-image analysis, Nat. Methods. 9 (2012) 676–682. doi:10.1038/nmeth.2019.

468 [33] D. Dai, D. Gu, Effect of metal vaporization behavior on keyhole-mode surface
469 morphology of selective laser melted composites using different protective
470 atmospheres, Appl. Surf. Sci. 355 (2015) 310–319. doi:10.1016/j.apsusc.2015.07.044.

471 [34] J.C. Haley, B. Zheng, U.S. Bertoli, A.D. Dupuy, J.M. Schoenung, E.J. Lavernia,
472 Working distance passive stability in laser directed energy deposition additive
473 manufacturing, Mater. Des. 161 (2019) 86–94. doi:10.1016/J.MATDES.2018.11.021.

474 [35] A.J. Pinkerton, Laser direct metal deposition: theory and applications in manufacturing
475 and maintenance, Adv. Laser Mater. Process. (2010) 461–491.
476 doi:10.1533/9781845699819.6.461.

477 [36] S.W. Wilkins, T.E. Gureyev, D. Gao, A. Pogany, A.W. Stevenson, Phase-contrast
478 imaging using polychromatic hard X-rays, Nature. 384 (1996) 335–338.
479 doi:10.1038/384335a0.

480 [37] F. Lia, J. Park, J. Tressler, R. Martukanitz, Partitioning of laser energy during directed
481 energy deposition, Addit. Manuf. 18 (2017) 31–39. doi:10.1016/j.addma.2017.08.012.

482 [38] Z.A. Munir, Surface Oxides and Sintering of Metals, Powder Metall. 24 (1981) 177–
483 180. doi:10.1179/pom.1981.24.4.177.

484 [39] M. Gharbi, P. Peyre, C. Gorny, M. Carin, S. Morville, P. Le Masson, D. Carron, R.
485 Fabbro, Influence of a pulsed laser regime on surface finish induced by the direct

metal deposition process on a Ti64 alloy, J. Mater. Process. Technol. 214 (2014) 485–495. doi:10.1016/j.jmatprotec.2013.10.004.

[40] M. Gharbi, P. Peyre, C. Gorny, M. Carin, S. Morville, P. Le Masson, D. Carron, R. Fabbro, Influence of various process conditions on surface finishes induced by the direct metal deposition laser technique on a Ti-6Al-4V alloy, J. Mater. Process. Technol. 213 (2013) 791–800. doi:10.1016/j.jmatprotec.2012.11.015.

[41] K.H. Richter, S. Orban, S. Nowotny, Laser cladding of the titanium alloy TI6242 to restore damaged blades, ICALEO 2004 - 23rd Int. Congr. Appl. Laser Electro-Optics, Congr. Proc. (2004). doi:10.2351/1.5060222.

[42] S. Tammas-Williams, H. Zhao, F. Léonard, F. Derguti, I. Todd, P.B. Prangnell, XCT analysis of the influence of melt strategies on defect population in Ti-6Al-4V components manufactured by Selective Electron Beam Melting, Mater. Charact. 102 (2015) 47–61. doi:10.1016/j.matchar.2015.02.008.

[43] J.E. Ramirez, B. Han, S. Liu, Effect of Welding Variables and Solidification Substructure on Weld Metal Porosity, 25 (1994) 2285–2294.

[44] L. Sinclair, C.L.A. Leung, S. Marussi, S.J. Clark, Y. Chen, M.P. Olbinado, A. Rack, J. Gardy, G.J. Baxter, P.D. Lee, In situ radiographic and ex situ tomographic analysis of pore interactions during multilayer builds in laser powder bed fusion, Addit. Manuf. 36 (2020) 101512. doi:10.1016/j.addma.2020.101512.

[45] S. Tammas-Williams, P.J. Withers, I. Todd, P.B. Prangnell, The Influence of Porosity on Fatigue Crack Initiation in Additively Manufactured Titanium Components, Sci. Rep. 7 (2017) 1–13. doi:10.1038/s41598-017-06504-5.

[46] S.S. L., The effect of laser power and traverse speed on microstructure, porosity and build height in laser-deposited Ti-6Al-4V, Scr. Mater. 43 (2000) 299.

[47] S. Bontha, N.W. Klingbeil, Thermal Process Maps for Controlling Microstructure in Laser-Based Solid Freeform Fabrication, SFF Proc. (2003) 219–226.

[48] H.L. Wei, T. Mukherjee, W. Zhang, J.S. Zuback, G.L. Knapp, A. De, T. DebRoy, Mechanistic models for additive manufacturing of metallic components, Prog. Mater. Sci. 116 (2021) 100703. doi:10.1016/j.pmatsci.2020.100703.

[49] A. V Catalina, S. Sen, D.M. Stefanescu, W.F. Kaukler, Interaction of porosity with a planar solid/liquid interface, Metall. Mater. Trans. A. 35 (2004) 1525–1538. doi:10.1007/s11661-004-0260-z.

[50] Q. Han, J.D. Hunt, Redistribution of Particles during Solidification, ISIJ Int. 35 (1995) 693–699. doi:10.2355/isijinternational.35.693.

Supplementary information:

1. Experimental set-up

A Blown Powder Additive Manufacturing Process Replicator (BAMPR) was developed to faithfully replicate a commercial DED-AM system whilst operating at a synchrotron[1]. The instrument was designed to be integrated into synchrotron beamlines, *e.g.* I12: Joint Engineering, Environmental, and Processing (JEEP) at Diamond Light Source[2]. The system is encapsulated within a Class I laser enclosure and comprises an inert environmental chamber, a high precision 3-axis platform, an industrial coaxial DED nozzle and a laser system. An industrial powder feeder (Oerlikon Metco TWIN-10-C) delivers powder to the system in a stream of argon gas. The laser is a 1070 nm Ytterbium-doped fibre laser beam (continuous-wave mode, laser power, P, of 0-200 W) which is coupled with tuneable optics to facilitate a focused spot size of between 50-700 μm. The spot size used in this study is 200 μm. The focal plane of the laser is set on the substrate surface. The substrate plate is positioned to be coincident with the focal plane of the laser beam. The laser is positioned to be concentric with the powder delivery stream blown from the nozzle and normal to the substrate plate. In this work the build platform was able to rotate continuously with a radius up to 50 mm, enabling traverse speed from 0 - 10 mm/s. The powder used was gas atomised Ti-6242 powder with a size distribution of 45 - 90 μm with a d_{50} of 70 μm. The substrate plate is positioned inside the environmental build chamber with X-ray transparent windows of Kapton internally and glassy carbon on the Class 1 enclosure. A 1 atm argon (99.999%) atmosphere is maintained with a flow of 6 L min^{-1} and the oxygen level is below 50 ppm during operation. The speed of the sample stages in this study was controlled to be between 1 to 5 mm s^{-1}. The speed range was set to enable a continuous track to be formed, as determined by preliminary laboratory trials. A 53 keV monochromatic X-ray beam was used for all trials and converted to visible light with a scintillator to capture as a radiographic video with a fast CMOS camera. The X-ray images were captured using a MIRO 310M camera (Vision Research Inc.) with a

548 pixel size of 3.24 µm at 200 fps. The resulting radiographic movies quantify the time-resolved
549 multi-layer melt track morphology evolution of Ti-6Al-2Sn-4Zr-2Mo (in wt%) (Ti6242) tracks on
550 Ti6242 substrates for a wide range of processing parameters during DED-AM builds.

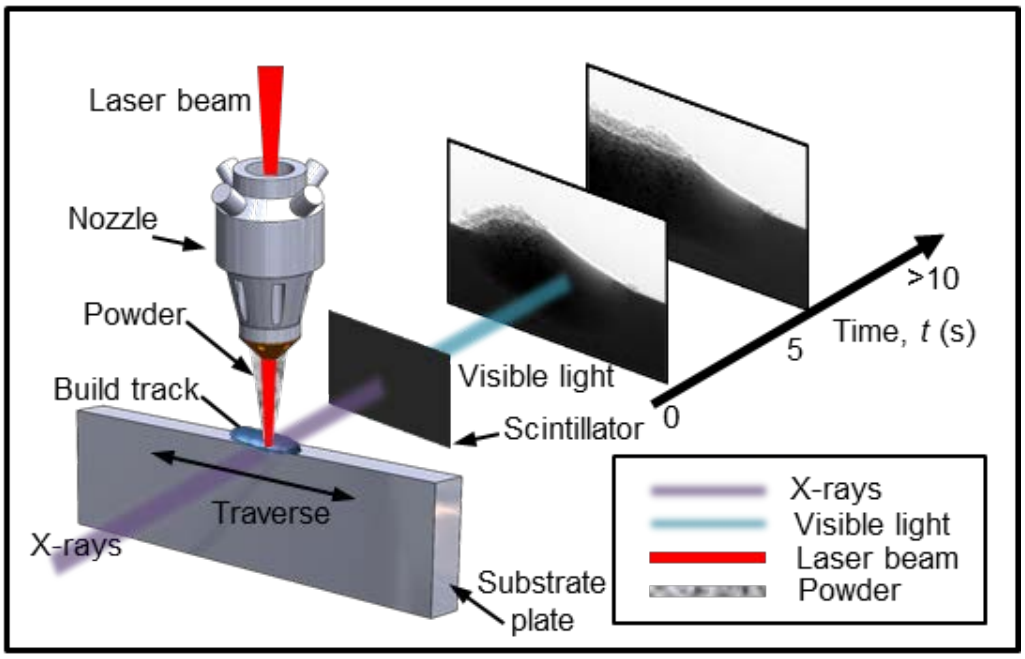

551

552 Supplementary Figure 1: Schematic of the in situ and operando X-ray imaging of DED AM of
553 Ti6242.

554 ## 2. Melt pool volume measurement

555 The melt pool volume was determined by assuming the melt pool to be ellipsoid-cap in shape.
556 Therefore, the apparent melt pool volume was calculated from the characteristic dimensions
557 (schematically illustrated in Supplementary Figure 1) according to:

558 $$V = \pi D_1(3L^2 + D_1^2) - \pi D_2(3L^2 + D_2^2)$$

559 (S1)

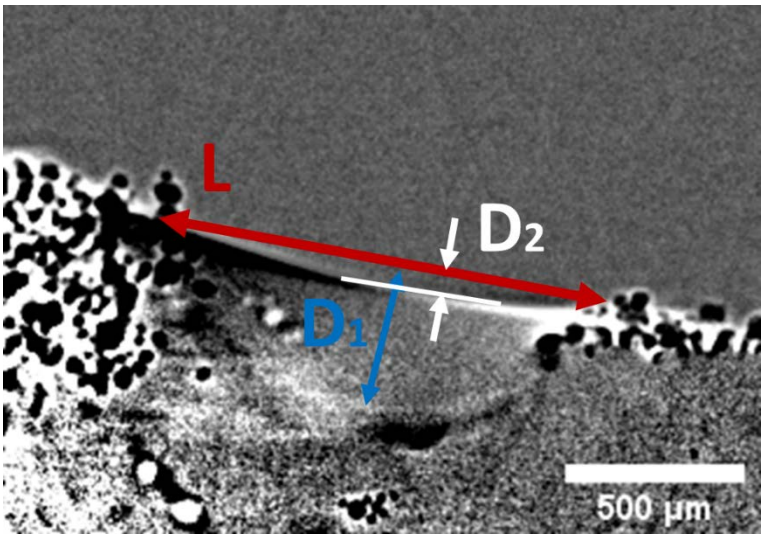

Supplementary Figure 2. Schematic of the melt pool volume calculation.

3. Sintering phenomenon

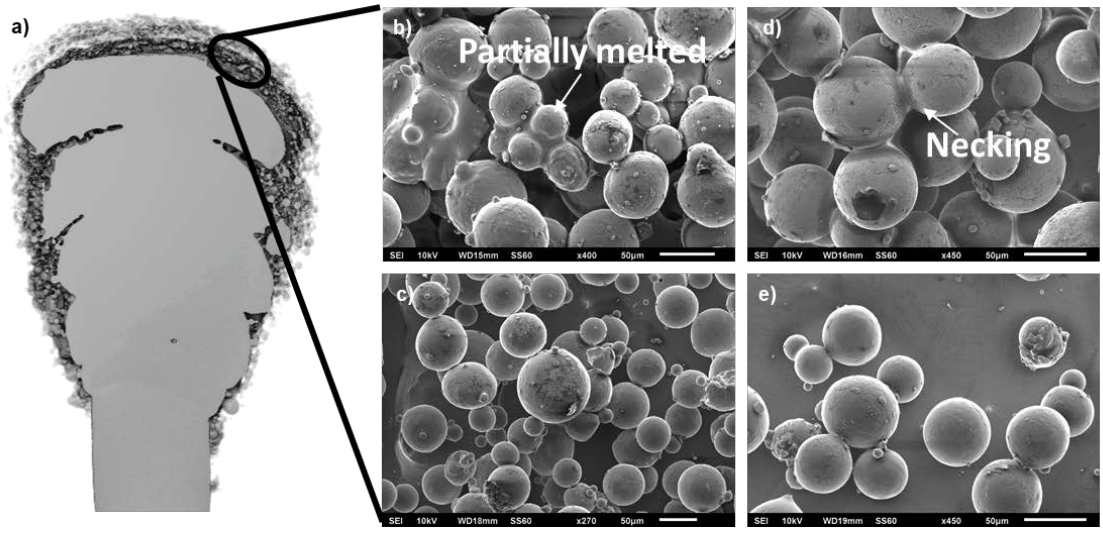

Supplementary Figure 3. Sintering phenomenon. (a) Cross-section of the melt-track from the micro-CT scan of Ti6242 melt-track revealing the lack of fusion between layers and the sinter particles. Parameters used were a traverse speed of 1 mm/s, a laser power of 200 W, and a powder feed rate of 1 g/min (b)-(e) Post-mortem SEM image of Ti6242 melt track surface showing with large numbers of particle necking and small proportions of partially melted particles attached to the melt-track. Scale bar = 50 µm.

4. Solidification behaviour of Ti6242

4.1 Thermal Model

The thin wall model reported by Vasinonta *et al.* [3–5] predicts the 2-dimensional heat flow during the deposition of thin walled blown powder DED builds with a laser heat source. This model essentially takes the thermal field prediction from half of the thin-plate model proposed by Rosenthal [6] with twice the heat input, Q.

$$\bar{T} = e^{-\bar{x}_0} K_0\left(\sqrt{\bar{x}_0{}^2 + \bar{z}_0{}^2}\right) \tag{S2}$$

$$\bar{T} = \frac{\pi k b (T - T_0)}{Q}, \qquad \bar{x}_0 = \frac{x_0 \rho C_p v}{2k}, \qquad \bar{z}_0 = \frac{z_0 \rho C_p v}{2k} \tag{S3-5}$$

Where, K_0 is the modified Bessel function of the second kind and zeroth order ρ, C_p and k are the density, specific heat capacity and thermal conductivity of solid, respectively. x_0 and z_0 are the co-ordinates, horizontal and vertical, in the reference frame and with the origin at the point heat source. Q, T_0 and T are the net heat input, base temperature, and predicted temperature and b is the width of the wall. It should be noted the following assumptions and simplifications are made:

Assumptions:

a) Line heat source
b) Heat of fusion is neglected
c) Melt convection is neglected
d) Material thermal properties independent of temperature

e) No heat loss from the workpiece surfaces

f) Infinitely tall workpiece

g) The process is steady state

h) Powder feeding is neglected

Considering the melt-pool boundary to be where $T = T_s$, in this work we fit the thermal model to experimental measurements of the melt pool length by solving for the parameter $^{Q}/_{b}$, such that the measured and predicted melt-pool lengths are equal.

Bontha et al. [7] expanded upon this work deriving the corresponding analytical equations for the cooling rate, $\frac{\partial T}{\partial t}$, cooling thermal gradient, *G* and solidification rate, *R*.

$$\frac{\partial \bar{T}}{\partial \bar{t}} = e^{-\bar{x}_0}\left\{\frac{\bar{x}_0}{\sqrt{\bar{x}_0{}^2 + \bar{z}_0{}^2}} K_1\left(\sqrt{\bar{x}_0{}^2 + \bar{z}_0{}^2}\right) + K_0\left(\sqrt{\bar{x}_0{}^2 + \bar{z}_0{}^2}\right)\right\} \tag{S6}$$

$$\frac{\partial \bar{T}}{\partial \bar{t}} = \frac{\partial T}{\partial t}\left(\frac{2\pi k^2 b}{Q\rho C_p v^2}\right) \tag{S7}$$

$$\bar{G} = \sqrt{\left(\frac{\partial \bar{T}}{\partial \bar{x}_0}\right)^2 + \left(\frac{\partial \bar{T}}{\partial \bar{z}_0}\right)^2} \tag{S8}$$

$$\frac{\partial \bar{T}}{\partial \bar{x}_0} = -e^{-\bar{x}_0}\left\{\frac{\bar{x}_0}{\sqrt{\bar{x}_0{}^2 + \bar{z}_0{}^2}} K_1\left(\sqrt{\bar{x}_0{}^2 + \bar{z}_0{}^2}\right) + K_0\left(\sqrt{\bar{x}_0{}^2 + \bar{z}_0{}^2}\right)\right\} \tag{S9}$$

$$\frac{\partial \bar{T}}{\partial \bar{x}_0} = -e^{-\bar{x}_0}\left\{\frac{\bar{z}_0}{\sqrt{\bar{x}_0{}^2 + \bar{z}_0{}^2}} K_1\left(\sqrt{\bar{x}_0{}^2 + \bar{z}_0{}^2}\right)\right\} \tag{S10}$$

611 $$\bar{G} = G\left(\frac{2\pi k^2 b}{Q\rho C_p v}\right)$$

612 (S11)

613

614 $$R = \frac{1}{G}\frac{\partial T}{\partial t}$$

615 (S12)

616 G and R are now computed using equations S12 for $T = T_s$ behind the deepest part of the
617 melt-pool *i.e.,* where the interface transitions from melting to solidification.

618 **4.2 Solidification Microstructure selection map**

619 The calculation that follows has been performed for v= 1 mm s^{-1} and P= 200 W, process
620 conditions.

621 First, using the well-known constitutional supercooling criterion for planar front stability is [8,9]
622 the G/R value for planar front growth is found to be given by equation S13

623 $$G_{Planar} = \frac{R\Delta T_0}{D_L}$$

624 (S13)

625 Where D_L is the diffusion coefficient for solute in the liquid and ΔT_0 is the equilibrium freezing
626 range of the alloy.

627 Data regarding solute diffusion coefficient in liquid titanium is scarce therefore has been
628 approximated as $\sim 1 \times 10^{-8}$ m^2s^{-1} [10] and solidification range ΔT_0 is set to 34 K for Ti6242
629 [11].

630 To further elucidate the nature of the solidification mode the limits of fully columnar and fully
631 equiaxed solidification have been evaluated according to Hunt [12] (eqns. S14-16).

632

633 $$G_{equiaxed} = 0.6{N_0}^{1/3}\Delta T_c\left(1 - \frac{{\Delta T_n}^3}{{\Delta T_c}^3}\right)$$

634 (S14)

635 $$G_{columnar} = 2.9{N_0}^{1/3}\Delta T_c\left(1 - \frac{{\Delta T_n}^3}{{\Delta T_c}^3}\right)$$

636 (S15)

637 $$\Delta T_c = \left(\frac{R}{a}\right)^{\frac{1}{n}}$$

638 (S16)

639 Where, N_0, is the nucleation density, ΔT_n is the undercooling a and n are material specific
640 parameters which are fit.

641 To the best of the authors' knowledge no reliable assessment of these parameters has been
642 undertaken for Ti6242. Therefore, in this case the experimentally calibrated curves for Ti-6Al-
643 4V [13] established by Kobryn and Semiatin are assumed to be approximately accurate for
644 Ti6242. Due to the uncertainty about the experimental value of ΔT_n in each case the condition
645 where $\Delta T_n = 0$ has also been extrapolated and potted in Supplementary Fig. 4 with dashed
646 lines.

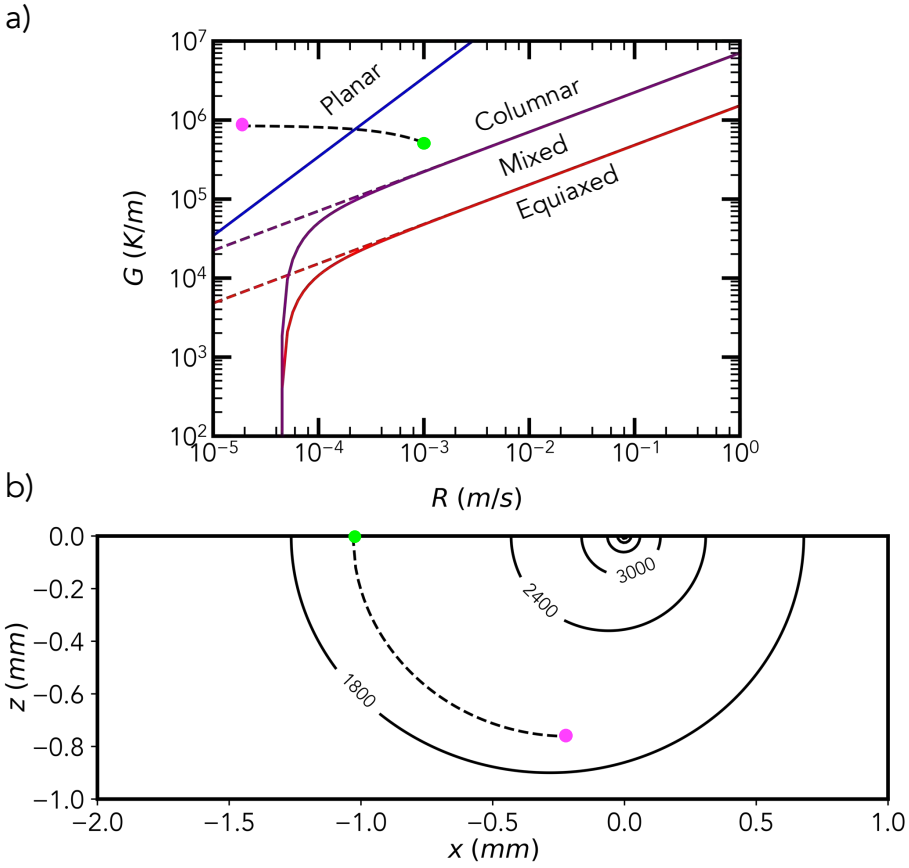

Supplementary Figure 4. a) Solidification microstructure selection map for Ti6242. Blue line represents the limit of planar front stability. The red and black lines correspond to limits for columnar dendritic and equiaxed dendritic growth, the dashed line black line indicates the changing values of G and v along the predicted solidification front isotherm as described in the Supplementary Information for process conditions of 1 mms^{-1} and 200 W. (linear energy density $200x10^3$ J/m). b) Calculated 2D steady state thermal field with temperature values in K. The dashed line in the insert shows the solid-liquid isotherm for 1 mm s^{-1}, 200 W process conditions.

Supplementary Figure 4 shows an approximate solidification microstructural selection map for dashed line black line indicates the predicted solidification front isotherm as described in the 2D thermal field inset for 1 mms^{-1}, 200 W, process condition. At the bottom of the melt-pool an initially planar solidification front is expected below a depth of 740 μm, above this a cellular-dendritic front is expected initially which will transition to an increasingly dendritic character

closer to the surface. It should be emphasised that this analysis corresponds to the mode of growth of the steady state solid-liquid front in the moving reference frame of the calculation.

References:

[1] Y. Chen, S. Clark, In situ and Operando X-ray Imaging of Directed Energy Deposition Additive Manufacturing, Sci. Adv. (n.d.).

[2] M. Drakopoulos, T. Connolley, C. Reinhard, R. Atwood, O. Magdysyuk, N. Vo, M. Hart, L. Connor, B. Humphreys, G. Howell, S. Davies, T. Hill, G. Wilkin, U. Pedersen, A. Foster, N. De Maio, M. Basham, F. Yuan, K. Wanelik, I12: The Joint Engineering, Environment and Processing (JEEP) beamline at Diamond Light Source, J. Synchrotron Radiat. 22 (2015) 828–838. doi:10.1107/S1600577515003513.

[3] A. Vasinonta, J. Beuth, M. Griffith, Process Maps for Laser Deposition of Thin-Walled Structures, Proc. 10th Solid Free. Fabr. Symp. (1999) 383–392.

[4] A. Vasinonta, J.L. Beuth, R. Ong, Melt Pool Size Control in Thin-Walled and Bulky Parts via Process Maps, Proc. 12th Solid Free. Fabr. Symp. (2001) 432–440.

[5] A. Vasinonta, J.L. Beuth, M. Griffith, Process Maps for Predicting Residual Stress and Melt Pool Size in the Laser-Based Fabrication of Thin-Walled Structures, J. Manuf. Sci. Eng. 129 (2007) 101. doi:10.1115/1.2335852.

[6] D. Rosenthal, The Theory of Moving Sources of Heat and Its Application to Metal Treatments, Trans. Am. Soc. Mech. Eng. 68 (1946) 849–866. doi:10.4236/eng.2011.32017.

[7] S. Bontha, N.W. Klingbeil, P.A. Kobryn, H.L. Fraser, Thermal process maps for predicting solidification microstructure in laser fabrication of thin-wall structures, J. Mater. Process. Technol. 178 (2006) 135–142. doi:10.1016/j.jmatprotec.2006.03.155.

[8] W.W. Mullins, R.F. Sekerka, Stability of a planar interface during solidification of a dilute

685 binary alloy, J. Appl. Phys. 35 (1964) 444–451. doi:10.1063/1.1713333.

686 [9] D.A. Huntley, S.H. Davis, Thermal effects in rapid directional solidification: linear theory,
687 Acta Metall. Mater. 41 (1993) 2025–2043.

688 [10] S.L. Semiatin, V.G. Ivanchenko, S. V. Akhonin, O.M. Ivasishin, Diffusion models for
689 evaporation losses during electron-beam melting of alpha/beta-titanium alloys, Metall.
690 Mater. Trans. B Process Metall. Mater. Process. Sci. 35 (2004) 235–245.
691 doi:10.1007/s11663-004-0025-5.

692 [11] A. Mitchell, A. Kawakami, S.L. Cockcroft, Segregation in titanium alloy ingots, High
693 Temp. Mater. Process. 26 (2007) 59–77. doi:10.1515/HTMP.2007.26.1.59.

694 [12] H.J. D., Steady state columnar and equiaxed growth of dendrites and eutectic, Mater.
695 Sci. Eng. 65 (1984) 75.

696 [13] P.A. Kobryn, S.L. Semiatin, Microstructure and texture evolution during solidification
697 processing of Ti-6A1-4V, J. Mater. Process. Technol. 135 (2003) 330–339.
698 doi:10.1016/S0924-0136(02)00865-8.

699

700